Original Research Article

International journal of spray and combustion dynamics

International Journal of Spray and Combustion Dynamics
2017, Vol. 9(4) 349–366

DOI: 10.1177/1756827717711015
journals.sagepub.com/home/scd
SAGE

Numerical issues in modeling combustion instability by quasi-1D Euler equations

Maria Luisa Frezzotti, Simone D'Alessandro, Bernardo Favini and Francesco Nasuti

Abstract

The present work is devoted to investigation of numerical issues related to combustion instability simulation through a quasi-1D Eulerian solver. The main aspects addressed are the choice of a suitable multispecies model and heat release response function formulation. Experimental data and high fidelity simulation results, available in literature, are reproduced with acceptable approximation. Main features of the flow field at limit cycle are shown. Moreover, a parametric study has been performed on time-lag response function characteristic parameters, leading to important conclusions on the pertinence of each assumption in the frame of a nonlinear tool.

Keywords

Longitudinal combustion instability, quasi-1D Euler equations, low-order models, monotonized thermodynamic model

Date received: 16 September 2016; accepted: 25 April 2017

1. Introduction

Design and development of new liquid rocket engines is a complex and challenging objective to pursue, where the impulse toward innovative solutions is often counterbalanced by the requirement of a reliable system, with proven capabilities of success. From this point of view, combustion instability is one of the most insidious phenomena to be controlled. Even if full-scale experimental campaigns have been performed,[1] with great improvement in the phenomenon knowledge, the required economical effort would be prohibitive today, with consequent necessity for alternative investigative procedures. As far as experiments are concerned, great interest is addressed to subscale test combustors,[2–5] requiring a more limited effort in terms of practical realization and allowing to achieve appreciable results in a relatively short time. Experiments are usually supported by simulations that can provide useful insight in the mechanisms sustaining instability and estimation of the quantities of interest. On the other hand, experimental data are necessary to validate numerical simulations and to assess the reliability of the selected model in describing the phenomenon of interest. Several approaches can be explored from the numerical point of view, according to the objective of the particular study. Nevertheless, it is important to remark that, in spite of the growing capabilities, the achievable computational effort can still be an issue for the study of combustion instability phenomena by detailed numerical models. For this reason, models like large eddy simulation, detached eddy simulation, or direct numerical simulation can hardly be considered as an option during the design phase of a new engine. Since the problem can be approached analytically only for very simplified cases, improvement and development of reliable low-order models appears to be a mandatory task for applications of practical interest. In this framework, an investigation on longitudinal combustion instability by a low-order nonlinear model is carried out in the present study according to the model by Smith et al.[6] More specifically, two formulations of multispecies quasi-1D Euler equations are considered: standard thermodynamics (ST) and monotonized thermodynamics (MOT), with the objective of identifying possible numerical issues and their consequences in the resulting modeling of combustion

Dipartimento di Ingegneria Meccanica e Aerospaziale, Sapienza, University of Rome, Rome, Italy

Corresponding author:
ML Frezzotti, Dipartimento di Ingegneria Meccanica e Aerospaziale, Sapienza, University of Rome, via Eudossiana 18, Rome 00184, Italy.
Email: marialuisa.frezzotti@uniroma1.it

instability. After evaluation of the scheme accuracy, of the role of spatial and temporal resolution and validation with exact Riemann problem solution, the continuously variable resonance combustor (CVRC) test case, designed and installed at Purdue University,[2,7–12] has been studied. The first part of the analysis points out differences between the two models, with particular attention to possible consequences in combustion instability applications. In the second part, the main features of limit cycle, according to experiments and data available in literature, are recovered, with a suitable choice of the response function (RF). Finally, particular attention is posed to sensitivity of results of CVRC test case to the choice of different models and parameters for the RF.

2. Quasi-1D Eulerian model

2.1. ST

A solver of multispecies quasi-1D Euler equations has been developed with the aim of including nonlinear regime in the study of combustion instability through simplified tools according to Smith et al.[6] In order to describe the physics of CVRC, combustion has to be taken into account. However, the present model does not describe combustion through equations for chemical kinetics but a simplified model has been implemented. First of all, in order to satisfy the mass balance, it is necessary that

$$\dot{\omega}_p - \dot{\omega}_o = \dot{\omega}_{fu} \tag{1}$$

where $\dot{\omega}_p, \dot{\omega}_o$, and $\dot{\omega}_{fu}$ are the rate of production per unit length of combustion products, oxidizer and fuel, respectively. In fact, combustion products are considered as a single species whose properties are computed with the chemical equilibrium code CEA.[13] Equation (1) can be expressed as a function of the OF ratio, i.e. the ratio between oxidizer and fuel mass flow rate

$$\dot{\omega}_p = \dot{\omega}_o \left(1 + \frac{1}{OF}\right) \tag{2}$$

As shown in equation (2), $\dot{\omega}_p$ and $\dot{\omega}_{fu}$ are both functions of $\dot{\omega}_o$. In order to simplify the model, only two species are considered: oxidizer and combustion products. Oxidizer is introduced at the left boundary of the oxidizer post (ox-post in Figure 1(a)) and consumed within a finite region of the chamber, identified by the abscissas l_s and l_f, where combustion is supposed to occur. In this zone of the chamber (see Figure 1(b)) oxidizer is consumed and replaced by combustion products, according to the proportion given in equation (2). The existence of fuel in the mixture before combustion is neglected. This assumption is justified because fuel contribution to mixture properties is of secondary importance for the present case. In fact, the distance between the fuel injection section and the reaction zone is small compared to the other characteristic dimensions of the engine and therefore taking into account for the presence of fuel in this region is not expected to have a major effect on wave propagation. The following simplifying hypothesis is then assumed: fuel is supposed to be injected in the region between l_s and l_f where it reacts instantaneously. For this reason only two species, oxidizer and combustion products, are needed to describe the system. In particular, as previously shown, production rates can be expressed as functions of $\dot{\omega}_o$

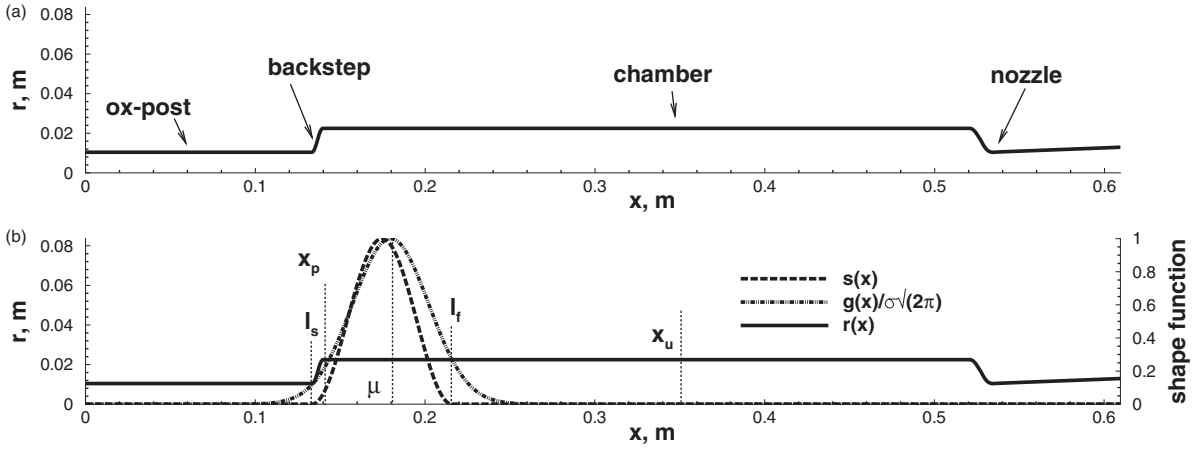

Figure 1. Geometry and source terms in CVRC as assumed in the quasi-1D computation. (a) Geometry of CVRC and (b) source term related to mass and, consequently, energy addition is limited by the two abscissas l_s and l_f and the associated shape function is represented with dashed line. The Gaussian distribution associated to response function is plotted with dash-dotted line. Sampling locations for pressure (x_p) and velocity (x_u) are pointed out. CVRC: continuously variable resonance combustor.

that is modeled as

$$\dot{\omega}_o = \beta \frac{\dot{m}_o}{l_f - l_s} Y_o(x,t) s(x) \tag{3}$$

where $\dot{m}_o$ is the oxidizer mass flow rate, $Y_o(x,t)$ is the oxidizer mass fraction, β is the minimum scalar value that allows to consume all the oxidizer in the space of the selected finite length combustion zone $(l_f - l_s)$ at steady state, and $s(x)$ is a shape function, defined as

$$s(x) = \frac{1}{2}\left[1 + \sin\left(-\frac{\pi}{2} + 2\pi \frac{x - l_s}{l_f - l_s}\right)\right] \quad \text{for} \quad l_s < x < l_f \tag{4}$$

and it is introduced to avoid discontinuities in the source terms.

Governing equations can be easily derived for ST model (see e.g. Law[14]) starting from continuity equation

$$(\rho A)_t + (\rho u A)_x = \dot{\omega}_p - \dot{\omega}_o \tag{5}$$

where ρ and u are mixture density and velocity, and A is cross sectional area. The second equation is continuity for the oxidizer

$$(\rho A Y_o)_t + (\rho u A Y_o)_x = -\dot{\omega}_o \tag{6}$$

where the minus sign at the right-hand side suggests that the source term is actually a consumption term. The last two equations are momentum and energy balance

$$(\rho u A)_t + \left[\left(\rho u^2 + p\right)A\right]_x = p A_x + u(\dot{\omega}_p - \dot{\omega}_o) \tag{7}$$

$$(\rho e_0 A)_t + (\rho u h_0 A)_x = (\dot{\omega}_p - \dot{\omega}_o)\left(h_0 + OF\Delta h_0^{rel}\right) + \dot{q}_{us} \tag{8}$$

where e_0 and h_0 are total internal energy and total enthalpy which include the kinetic energy $u^2/2$ and are linked to pressure and density via the perfect gas relationship $(R = \sum R_i Y_i, c_p = \sum c_{p_i} Y_i$ and $\gamma = c_p/(c_p - R)$ with c_p and c_v specific heat at constant pressure and volume, respectively and R gas constant), Δh_0^{rel} is the heat of reaction per unit mass of oxidizer, released by chemical reactions. The term $\dot{q}_{us}$ refers to unsteady heat release contribution. More precisely, it represents the RF through which the model takes into account the effect of flow field oscillations on combustion. This effect is modeled according to Crocco and Cheng[15] expressing the unsteady part of heat release as function of the pressure (equation (9)) or velocity (equation (10)) sampled at a specific abscissa (x_p or x_u, almost coincident with the antinode of the first longitudinal modal shape), with a certain time lag τ_p, in the case of pressure time-lag formulation, or τ_u, for velocity time-lag formulation. Values of τ_p and τ_u depend on the selected abscissa x_p and x_u, respectively

$$\dot{q}_{us}(x,t) = \frac{e^{-\frac{(x-\mu)^2}{2\sigma_p^2}}}{\sqrt{2\pi\sigma_p^2}} \alpha_p A(x)\left[p(x_p, t - \tau_p) - \bar{p}_f(x_p)\right] \tag{9}$$

$$\dot{q}_{us}(x,t) = \frac{e^{-\frac{(x-\mu)^2}{2\sigma_u^2}}}{\sqrt{2\pi\sigma_u^2}} \alpha_u A(x)[u(x_u, t - \tau_u) - \bar{u}(x_u)] \tag{10}$$

The overlined values are the time averaged values, μ and σ_p (or σ_u) are mean value and standard deviation of the Gaussian distribution assumed as shape function (Figure 1(b)) for the pressure time lag (or velocity time lag) response. A Gaussian shape function has been introduced for $\dot{q}_{us}$ to avoid discontinuities in the unsteady heat release source term and emphasize its statistical aspect. The selected shape function allows one to select a given "combustion" profile in a well-defined region.[6] The amount of heat released due to pressure or velocity oscillation is controlled by a proportionality factor of RF intensity α_p (or α_u), in analogy with the interaction index n in Crocco's $n - \tau$ formulation. Figure 1 shows the geometry, assumed for the quasi-1D computation, and the shape functions associated to the different source terms. Boundary conditions are fixed oxidizer mass flow rate ($\dot{m}_{o,0}$) and stagnation temperature (T_0) at the inlet and a choked nozzle with a supersonic outflow.

In order to identify resonance frequencies, a disturbance must be introduced in the system for observing its response. Different quantities can be perturbed; one of the most common approaches is to perturb mass flow rate at the inflow boundary.[4,16–18] If mass flow rate is forced with a multisine signal, the disturbance can be expressed as

$$\dot{m}_o(t) = \dot{m}_{o,0}\left[1 + \sum_{k=1}^{K} \delta \sin(2\pi(f_0 + k\Delta f)t)\right] \tag{11}$$

where f is the frequency, $\Delta f = 50\,\text{Hz}$ is the frequency resolution, $f_0 = 50\,\text{Hz}$ is the minimum frequency, and $K = 140$ is the number of considered frequencies, providing also the maximum frequency in the signal of 7000 Hz. A lower value of Δf has been tested ($\Delta f = 10\,\text{Hz}$) yielding to the same results in terms of resonance frequencies and showing that the range up to 7000 Hz with resolution of 50 Hz allows to get the complete spectrum of the response to disturbance. Since the period of the multisine signal is $1/\Delta f$, the coarser frequency resolution has been assumed in order to reduce the computational time. If the amplitude δ is a small

percentage of the mean value (less than 0.1%), a small variation in the solution, with respect to the steady state case, is expected and the system response can be most likely considered linear for a small interval of time. The same happens if the perturbation is characterized by a single frequency f_s

$$\dot{m}_o(t) = \dot{m}_{o,0}[1 + \delta \sin(2\pi f_s t)] \tag{12}$$

Alternatively to the perturbation of inflow mass flow rate, the disturbances described in equations (11) and (12) are also applied on the mass flow rate source term (equation (3)) instead of boundary condition.

2.2. MOT

MOT model is a generalization of the model presented by Abgrall[19] and differs from ST for the replacement of equation (6) with a set of three equations (equations (13), (15), and (16)), derived from energy balance.[20] In particular, Abgrall[19] pointed out the presence of spurious pressure oscillations in the case of multispecies handled with finite volume schemes using ST model. However, it is possible to observe that the same behavior is typical also of temperature and speed of sound in the same conditions. MOT model is capable of assuring monotonic behavior of all the above-mentioned quantities.

The energy balance (equation (8)) can be written in different forms, expressing internal energy e as a function of pressure, temperature, or speed of sound

$$\rho e = \frac{p}{\gamma - 1} = \rho c_v T = \frac{\rho a^2}{\gamma(\gamma - 1)}$$

The three forms of energy equation are redundant in the analytical model but their integration in the numerical model is needed to assure monotonic behavior of pressure, temperature, and speed of sound. The equations to be considered are written in the following

$$\eta_t + \tilde{u}\eta_x = \dot{\eta} \tag{13}$$

where

$$\tilde{u} := \frac{\langle pu \rangle}{\bar{p}} \approx \frac{\langle pu \rangle}{\langle p \rangle} \tag{14}$$

$$(\rho c_v A)_t + (\rho u c_v A)_x = (\dot{\omega}_p - \dot{\omega}_o)\left[(1 + OF)c_{v,p} - OFc_{v,o}\right] \tag{15}$$

$$(\rho \zeta A)_t + (\rho u \zeta A)_x = (\dot{\omega}_p - \dot{\omega}_o)\left[(1 + OF)\zeta_p - OF\zeta_o\right] \tag{16}$$

where γ is the ratio between specific heat at constant pressure and constant volume

$$\eta = \frac{1}{\gamma - 1}, \quad \zeta = \frac{\eta}{\gamma}$$

At steady-state condition (identified with the subscript *ss*)

$$\dot{\eta}|_{ss} = \tilde{u}\eta_x \tag{17}$$

From continuity equation, at the same condition

$$(\rho u A)_x = \dot{\omega}_p - \dot{\omega}_o \tag{18}$$

The mass flow rate at a generic axial position can be obtained defining

$$\Omega(x) := \int_{l_s}^{x} \left[\dot{\omega}_p(\hat{x}) - \dot{\omega}_o(\hat{x})\right] \mathrm{d}\hat{x} \tag{19}$$

that yields to the definition of the mass flow rate $\dot{m}$ at a generic abscissa

$$\dot{m}(x) = \Omega(x) + \dot{m}_{o,0} \tag{20}$$

and, consequently, Y_o, γ, and η can be written

$$Y_o(x) = 1 - \frac{1 + OF}{1 + \frac{\dot{m}_{o,0}}{\Omega(x)}} \tag{21}$$

$$\gamma(x) = \frac{c_{p,o}Y_o(x) + c_{p,p}(1 - Y_o(x))}{c_{v,o}Y_o(x) + c_{v,p}(1 - Y_o(x))} \tag{22}$$

$$\eta(x) = \frac{1}{\gamma(x) - 1} = \frac{Y_o(x)\left(c_{v,o} - c_{v,p}\right) + c_{v,p}}{Y_o(x)\left(R_o - R_p\right) + R_p} \tag{23}$$

where R is the gas constant.

Computing the space derivative and defining $\Delta R = R_o - R_p$, $\Delta c_v = c_{v,o} - c_{v,p}$ and $\Delta c_p = c_{p,o} - c_{p,p}$

$$\eta_x(x) = \frac{Y_{o,x}(x)\left(\frac{R_p}{\Delta R} - \frac{c_{v,p}}{\Delta c_v}\right)}{Y_o^2(x)\frac{\Delta R}{\Delta c_v} + \frac{R_p^2}{\Delta R \Delta c_v} + \frac{2Y_o(x)R_p}{\Delta c_v}} \tag{24}$$

Substituting equations (14) and (24) in equation (17) the source term for equation (13) is given. Boundary conditions are the same of the previous case: fixed mass flow rate and stagnation temperature at the left boundary and choked nozzle on the right.

Resonant frequencies and modal shapes are computed as described for the ST model. In both cases

the Godunov-like integration scheme, second-order accurate in space and time, has been implemented. An exact Riemann solver, modified for multispecies, has been implemented according to Gottlieb et al.[21]

From the mathematical point of view, the obtained system of equations preserves the fundamental properties of the system of Euler equations, being hyperbolic, with the same characteristic directions, and allowing the existence of disturbances of the same nature: rarefaction, compression and shock waves on the $(u + a)$ and $(u - a)$ families, and contact discontinuities on the u family.[20]

Table 1. Contact discontinuity test case. Initial condition and thermodynamic properties of oxygen and products of combustion with hydrogen.

	Oxygen	Combustion products
p (MPa)	6	6
ρ (kg/m^3)	76.97	1.34
T (K)	300	3556
u (m/s)	159.62	159.62
γ	1.51	1.14

3. Test case for multispecies: Contact discontinuity

Differences between the two models are first investigated through an elementary test case: a straight duct with a contact discontinuity for which the exact solution can be analytically computed since the discontinuity moves at the flow velocity (see Gottlieb et al.[21] and Toro[22]). In particular, the discontinuity is both in terms of temperature and species. The considered gases are oxygen, on the left half of the duct, and the mixture obtained from the combustion of oxygen and hydrogen, on the right half. The mixture properties have been computed with CEA[13] assuming oxidizer temperature at the inflow 300 K, hydrogen temperature 280 K, chamber pressure 6 MPa, and OF ratio 6. The properties of oxygen and combustion products mixture are summarized in Table 1, giving the initial condition for the selected test.

Exact solution is represented in Figure 2 for the sake of comparison, showing a discontinuity of density and mass fraction, moving at the same velocity of the flow.

Results for ST and MOT models are compared with the exact solution in Figure 2. The ST model, differently from MOT, exhibits spurious pressure waves of quite high intensity. Velocity and density also show a nonmonotonic behavior that is inconsistent with the exact solution.

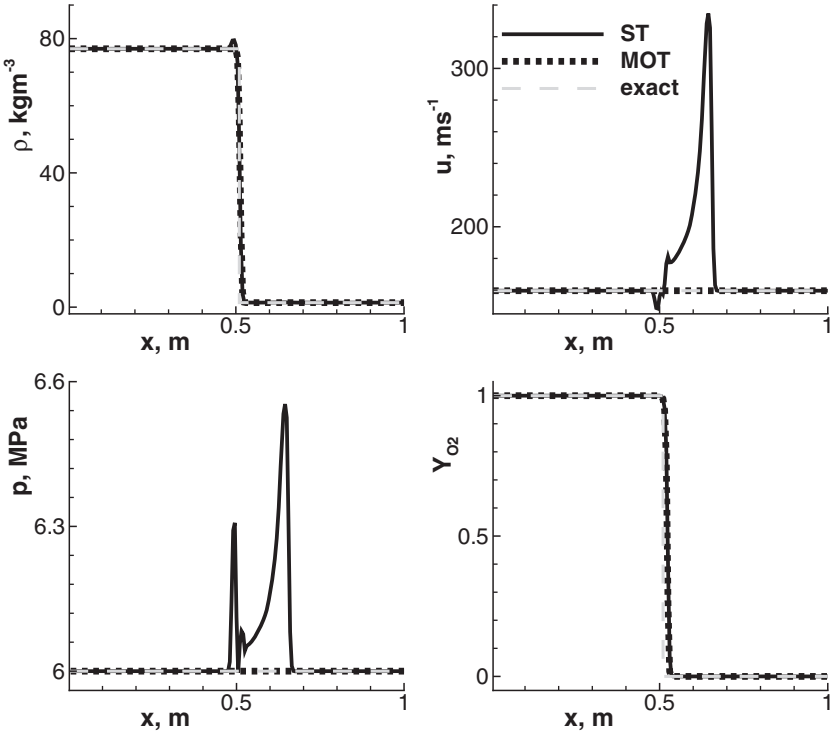

Figure 2. Solution of the contact discontinuity test case at time 65 μs computed with MOT, ST, and exact solution. MOT: monotonized thermodynamics; ST: standard thermodynamics.

The results of this test case show that the ST model applied to the present quasi-1D finite volume solver can produce spurious pressure waves, if species with different molecular weight are considered. This effect is not observed in the MOT model, whose formulation is built to integrate the mixture of thermodynamic properties and, consequently, to obtain the correct pressure value.

Table 2. CVRC operating conditions.

Parameter	Value
Fuel mass flow rate (kg/s)	0.027
Fuel temperature (K)	300
Oxidizer mass flow rate (kg/s)	0.320
Oxidizer temperature (K)	1030
Oxidizer percent H_2O	57.6
Oxidizer percent O_2	42.4
Equivalence ratio	0.8
Oxidizer post length (m)	0.14

CVRC: continuously variable resonance combustor.

4. CVRC test case

The selected test case is the CVRC combustor, which consists of a cylindrical chamber and a single coaxial injector where propellants are hydrogen peroxide (90% H_2O_2 and 10% H_2O), dissociated on a catalyst bed, and methane. The peculiar characteristic of CVRC is the variable length of the oxidizer post, from 0.089 to 0.191 m, realized by a translating shaft. The slots through which propellants are injected in the chamber are choked in normal operating conditions, providing an acoustic boundary from the manifold. Several tests have been carried out, considering both fixed and variable post length. Further details on the experiment can be found in literature, e.g. Yu et al.[9] and Selle et al.,[23] while a brief summary of operating condition is given in Table 2.

4.1. Steady-state solution

A preliminary investigation on grid resolution has been performed according to Roache[24] to verify grid convergence, leading to the choice of an equally spaced grid of 1050 cells. For CVRC combustor, the steady-state solution has been computed with both models, ST and MOT, and assuming $\dot{q}_{us} = 0$.

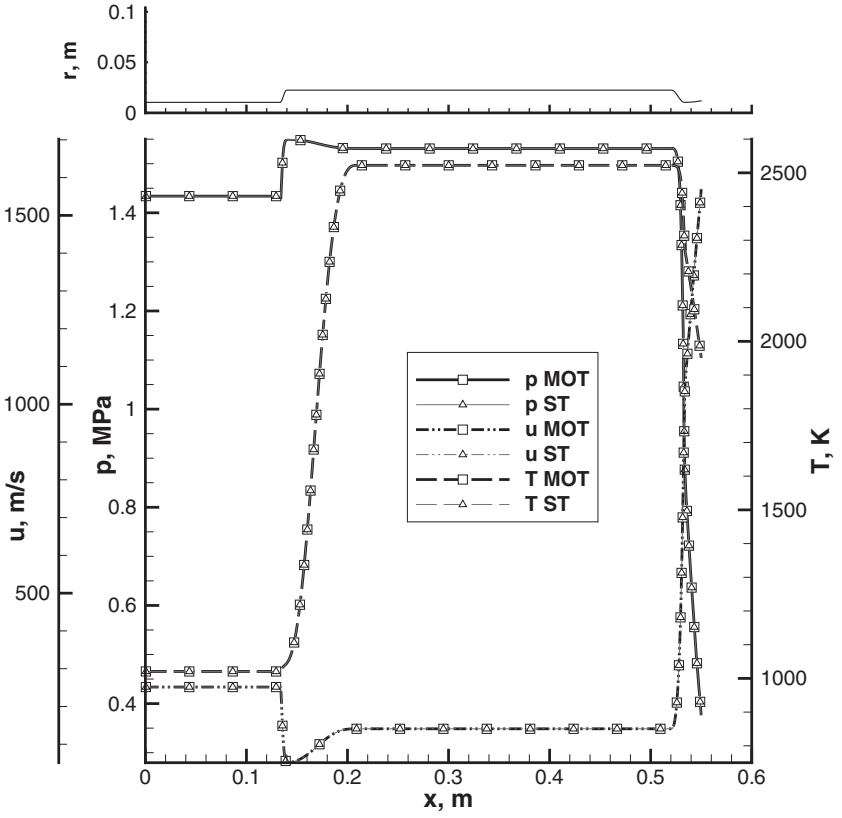

Figure 3. Geometry (top) and steady-state solution for CVRC combustor computed with MOT and ST (bottom). CVRC: continuously variable resonance combustor; MOT: monotonized thermodynamics; ST: standard thermodynamics.

Results for the steady-state computation with ST and MOT models are basically coincident, as shown in Figure 3.

4.2. Chamber resonance frequencies

To determine the chamber resonance frequencies by the present simulation model, the system is perturbed with small amplitude disturbances characterized by multiple frequencies, and still assuming $\dot{q}_{us} = 0$. In these conditions, if perturbations are sufficiently small, the system behaves as it were linear, even if governing equations are nonlinear. In this linear regime, in absence of mean flow, if the system is perturbed with a small amplitude disturbance at resonance frequency, the observed response amplitude should grow in time. Differently, the presence of mean flow causes the excited system to act like a damped harmonic oscillator and the disturbance does not grow indefinitely. In fact, stable oscillations are reached because of energy losses through the boundaries, which keep perturbations in the linear regime. Here small perturbations are introduced on the oxidizer mass flow rate, according to equations (11) and (12). The power spectral density (PSD) of pressure obtained perturbing the oxidizer mass flow rate boundary condition or mass flow rate source term with multisine allows to identify the resonance frequencies (see Figure 4). ST and MOT formulations give comparable results.

Analyzing the system response (Figure 4) it is possible to notice that only some of the resonance frequencies are observed with comparable intensity in both kinds of perturbation. In particular, the dominant frequency for all the presented spectra is observed at 1500 Hz. Note that, as will be shown in the following, this frequency (within a few Hz tolerance) is the dominant one also in nonlinear regime. The other peaks correspond to different resonance frequencies and modal shapes. A detailed discussion of linear regime and modal shapes is beyond the purposes of the present work; however, it is worth noticing that in some cases the resulting modal shape is affected by the kind of perturbation.

4.3. Nonlinear regime

In real systems, in presence of local fluctuations of propellant mass flow rate, pressure, and velocity, the system reacts with corresponding fluctuations of heat release that in turn can affect the oscillating behavior of the system. In these conditions, oscillations can easily grow up and tend to diverge in case of resonance. Oscillation growth is usually controlled by nonlinear effects that appear for oscillation over a certain threshold level and are able to limit the oscillation that becomes stable in the form of the so-called limit cycle. Combustion instabilities can be therefore considered as those characterized by limit cycles of intolerable amplitude. It is therefore necessary to investigate the system response in nonlinear regime and this has been done considering the two different formulations of time-lag RF, reported in equations (9) and (10), respectively. Note that, even if the RF formulation is linear, being based on pressure or velocity fluctuations, nonlinear limit cycle can be reached due to nonlinearities embedded in Euler equations, yielding nonlinear wave propagation as long as energy transfer between different modes. The parameters to be included in the characterization of RFs have been taken according to Frezzotti et al.[25,26] and are listed in Table 3. These parameters have been inferred by the results of the two-dimensional simulations performed by Sardeshmukh et al.[27] In particular, the sampling location for pressure and velocity, x_p and x_u, have been chosen at the antinode of the first

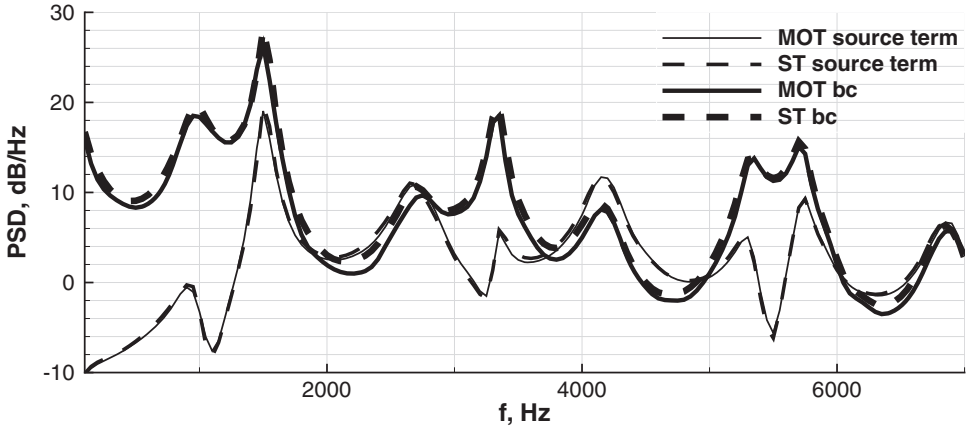

Figure 4. PSD of the pressure signal computed with MOT and ST applying a multisine forcing on oxidizer mass flow rate boundary condition (bc) and mass flow rate source term (source term). The probe is at $x = 0.508$ m. MOT: monotonized thermodynamics; PSD: power spectral density; ST: standard thermodynamics.

longitudinal mode for pressure and velocity, respectively. The time lag has been estimated evaluating the cross-correlation between the signal of pressure or velocity, in the case of pressure time lag and velocity time lag, respectively, and the heat release rate integrated in the chamber. It represents the distance in time between the peak of pressure or velocity at the sampling location and the peak of heat release rate. The mean of the Gaussian distribution, $\mu_p = \mu_u = \mu$, has been selected as the location of maximum heat release rate and, finally, the values of proportionality index, i.e. α_p or α_u, and the standard deviation, i.e. σ_p or σ_u, have been selected minimizing a suitable cost function, representing the difference between heat release rate computed with quasi-1D and 2D high fidelity simulations.

Table 3. Parameters extracted by Frezzotti et al.[25,26] from 2D-axisymmetric simulations performed by Sardeshmukh et al.[17]

Pressure time lag		Velocity time lag	
μ_p (m)	0.180	μ_u (m)	0.180
x_p (m)	0.138	x_u (m)	0.355
τ_p (ms)	0.620	τ_u (ms)	0.475
α_p (m/s)	1960	α_u (kPa)	2970
σ_p (m)	0.0424	σ_u (m)	0.0224

The procedure for the computation of the nonlinear regime is carried out in three steps:

1. The steady state has to be computed.
2. Then, a small amplitude perturbation, characterized by a single frequency, is applied at the oxidizer mass flow boundary condition.
3. The perturbation is interrupted and the RF is activated.

In steps 1 and 2 $\dot{q}_{us} = 0$ while in step 3 $\dot{q}_{us} \neq 0$. If step 2 is carried out up to the same final time, considering two different frequencies of the perturbation, the initial conditions at step 3 will be different.

As the limit cycle frequency given by the 1D simulation is one of the unknown of the problem, an assumption has to be made about the selection of the time-lag value τ_p to keep the phase constant. The approach followed in the present work (Figure 5)

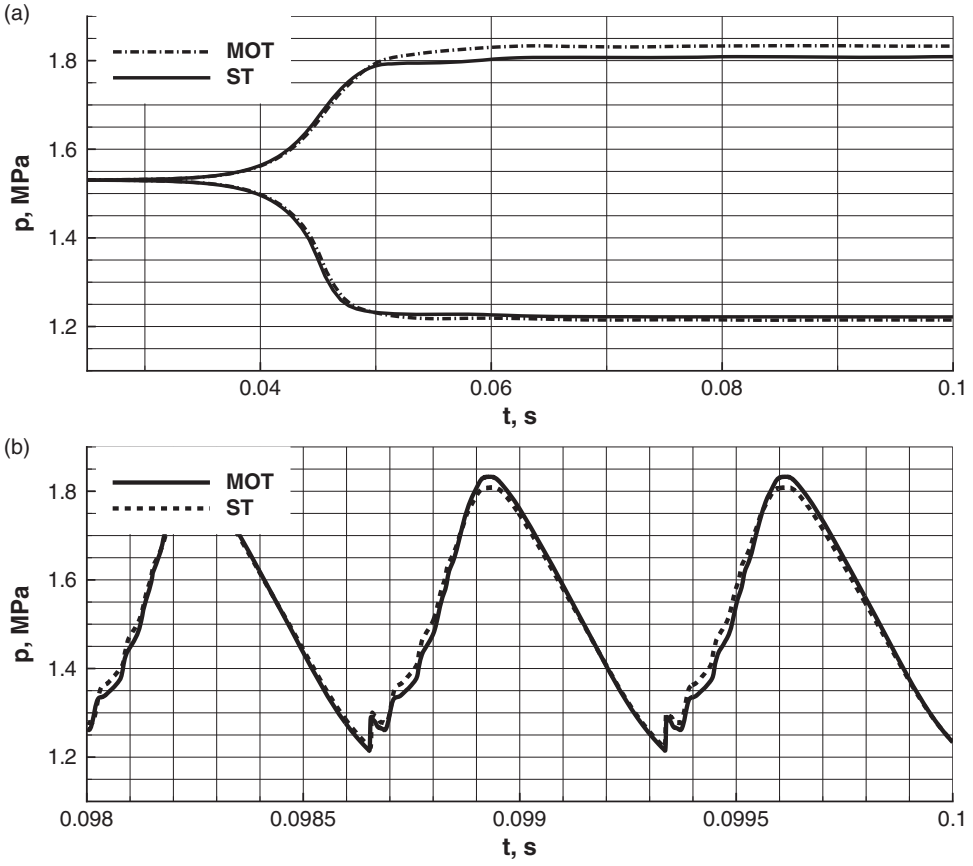

Figure 5. Comparison between ST and MOT at limit cycle using pressure time-lag response function. (a) Limit cycle envelope and (b) enlargement on pressure signals. MOT: monotonized thermodynamics; ST: standard thermodynamics.

estimates the time period T computing, at runtime, the approximated frequency $f = 1/2L\frac{1}{L}\int_0^L a(x,t)\mathrm{d}x$ where L is the length of the chamber and a the speed of sound. The reason for a runtime evaluation is the possible change of T in nonlinear regime. With this second approach f changes from 1390.55 Hz at the beginning of the computation up to 1383.07 Hz when limit cycle is reached and as a consequence τ_p from 0.669 to 0.672 ms.

The results obtained with either RF based on pressure and velocity, respectively, and using ST and MOT model are now discussed. Pressure time history at $x = 0.508$ m, just upstream of the nozzle, is shown in Figures 5 and 6. It is remarked that from now on, all the presented pressure signals are relative to this abscissa.

Independently of the used RF, the differences between the thermodynamic models in terms of pressure oscillation amplitude are small (0.05 MPa) and the wave form is similar, with a quite steep front of compression and a smooth rarefaction.

PSD of pressure signal at nozzle entrance is shown for the case of pressure (Figure 7) and velocity (Figure 8) time-lag response. The same frequencies are observed with MOT and ST model and, moreover, the two models show a very similar distribution of power density on the different harmonics.

Table 4 summarizes the frequencies observed at limit cycle using pressure and velocity time-lag RF. The values are compared with experimental and multidimensional data reported by Sardeshmukh et al.[27] and Harvazinski et al.[10]

Computing the PSD of pressure signals at limit cycle, it is possible to clearly identify the resonance frequencies whose values are in good agreement with those obtained by numerical simulations from which RF parameters have been extracted.[27] This proves that quasi-1D model is able to reproduce the multidimensional behavior in terms of frequency response.

Also in terms of amplitude of limit cycle and wave form, experimental and numerical results summarized by Sardeshmukh et al.[27] are comparable with quasi-1D simulations shown in Figures 5 and 6. In fact, the experimental amplitude at limit cycle is about 0.8 MPa. Discrepancies with experimental data are not surprising as they are in line with those of CFD results used to calibrate RFs.

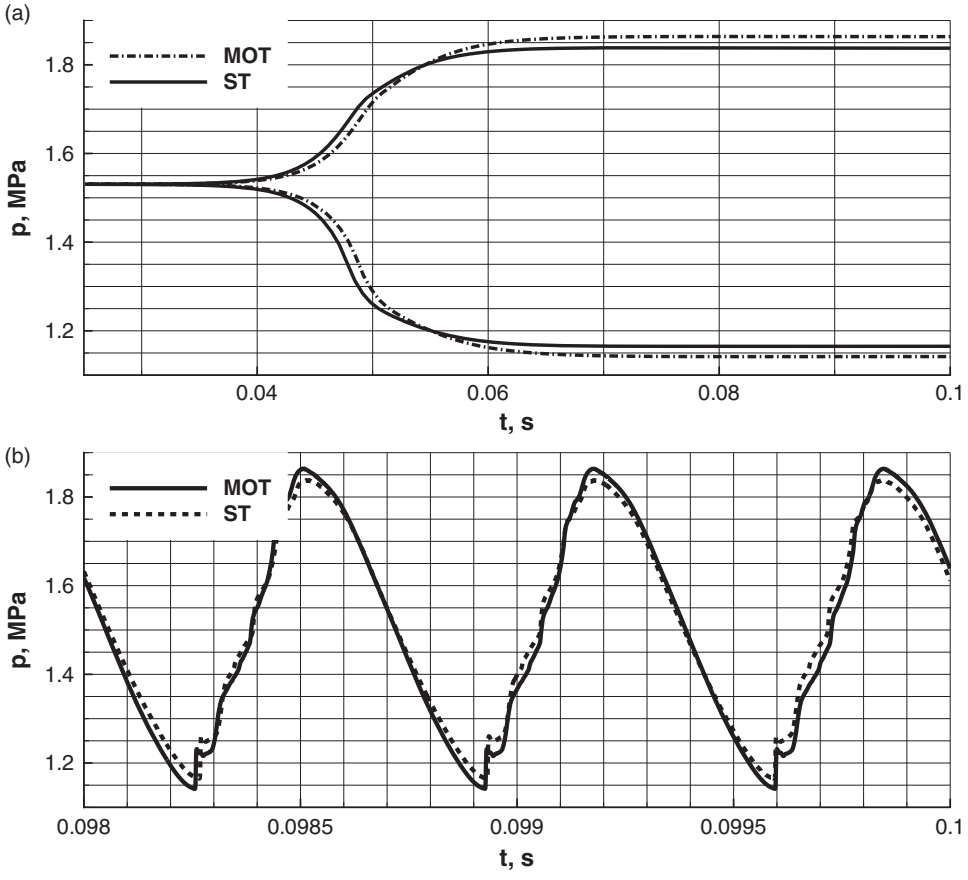

Figure 6. Comparison between ST and MOT at limit cycle using velocity time-lag response function. (a) Limit cycle envelope and (b) enlargement on pressure signals. MOT: monotonized thermodynamics; ST: standard thermodynamics.

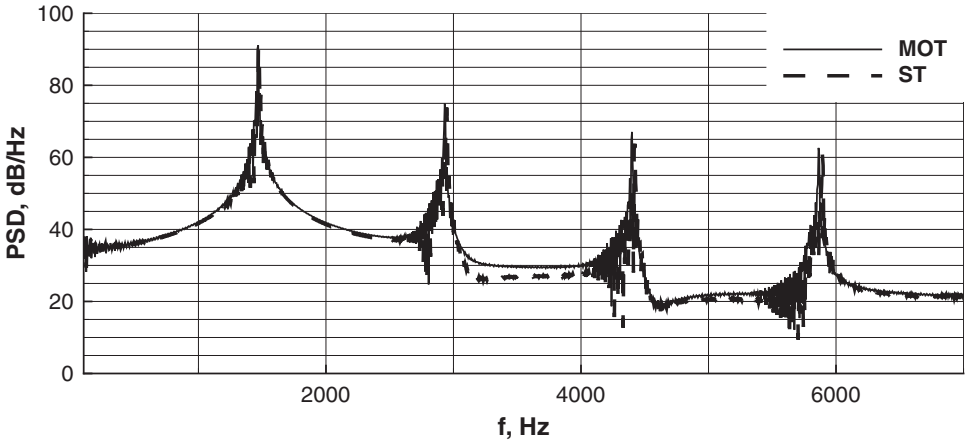

Figure 7. Pressure PSD. Comparison between ST and MOT using pressure time-lag response function. MOT: monotonized thermodynamics; PSD: power spectral density; ST: standard thermodynamics.

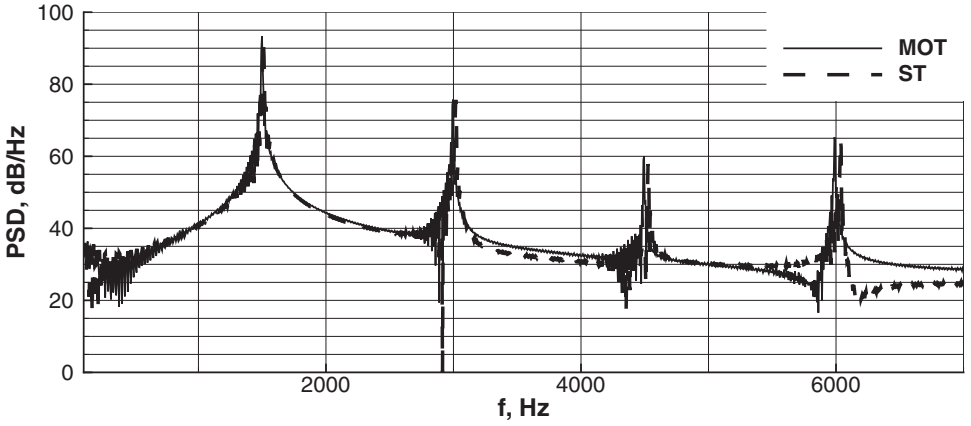

Figure 8. Pressure PSD. Comparison between ST and MOT using velocity time-lag response function. MOT: monotonized thermodynamics; PSD: power spectral density; ST: standard thermodynamics.

Table 4. Comparison between experimental and numerical frequencies. All data from experiments[10] and multidimensional simulations (2D by Sardeshmukh et al.[27] and 3D by Harvazinski et al.[10]) and quasi-1D analysis refer to limit cycle.

		1D			
	Experimental	Pressure time lag	Velocity time lag	2D	3D
f_1, Hz	1324	1469	1498	1520	1571
f_2, Hz	2655	2931	2997	3039	3114
f_3, Hz	3979	4400	4495	4519	4685

Finally, observing the results it is possible to conclude that the two thermodynamical models are equivalent for the present test case. This confirms the validity of MOT model as a general approach that could be particularly useful dealing with finite volumes schemes, when multiple species with very different thermodynamic properties have to be taken into account. However, since the two models are substantially equivalent for the case of CVRC application, the ST model is used hereinafter.

4.3.1. Limit cycle description. The nonlinear analysis carried out so far allowed to reproduce the limit cycle with reasonable approximation in terms of amplitude, frequency, and pressure signal at the selected probe (reference experimental data and high fidelity simulations results are shown by Sardeshmukh et al.[27]). In the present section, the main features of limit cycle are described using the obtained temperature, pressure, and velocity fields, shown in Figure 9, at different instances within one cycle. Images refer to the case of velocity time-lag response, where the parameters have been characterized according to the previous section

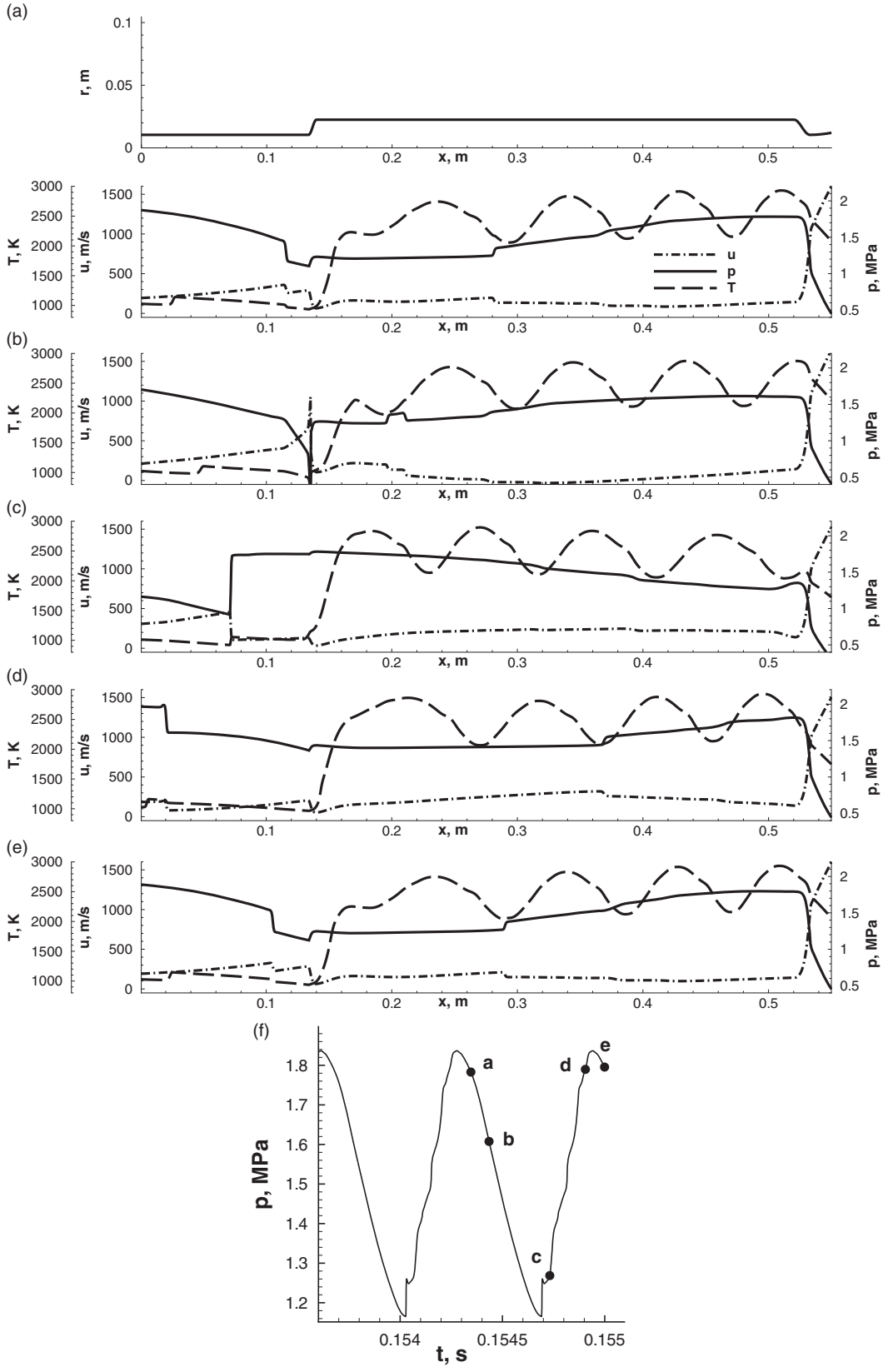

Figure 9. Sequence of time instants within one cycle of pressure, velocity, and temperature at limit cycle. On the top of the first plot geometry is represented. Pressure at $x = 0.508$ m is shown, singling out the times represented in the selected snapshots. (f) Pressure signal at $x = 0.508$ m.

(see Table 3). Observing pressure and velocity distributions in space (see Figure 9) it is possible to conclude that oscillations are occurring at the first longitudinal mode.

In fact, the flow field is characterized by traveling pressure waves leading to a global behavior similar to a standing wave occurring at the first longitudinal mode. Figure 9(a) shows the presence of a shock wave, moving downstream in the oxidizer post while another shock, of lower intensity, travels upstream in the chamber. When the first shock interacts with the area variation at the step, a sonic expansion is reflected while, in the chamber, a compression of lower intensity interacts with the shock traveling upstream (Figure 9(b)) and velocity reaches its minimum value, changing its sign. It is noteworthy that, even if an expansion is expected, the magnitude of the phenomenon is overestimated. In fact, multidimensional simulation results show that the expansion leads to a maximum Mach number of 0.7. A certain discrepancy in the region of the step has to be expected since in that zone, multidimensional effects are not negligible. In particular, the hot gas recirculation zone at the back step, leading to a radial temperature and velocity gradient, is not represented in the quasi-1D model. Moreover, 2D[27] and 3D simulations[10] show that the shock is actually normal in the oxidizer post, while, this is not the case after it passes the step and arrives in the chamber, where the shock profile becomes curve. In Figure 9(c) it is shown that the resulting system of waves generates a shock wave, moving upstream in the oxidizer post, that is able to suppress the sonic expansion while pressure waves of low intensity travel downstream in the chamber. In Figure 9(d) the shock wave in the oxidizer post and the compression in the chamber have been reflected at the boundaries, yielding to a shock, moving downstream in the post, and a compression, traveling upstream in the chamber. As far as temperature field is concerned, it can be noticed that oscillations due to variation of heat release rate, induced by the RF, propagate with the flow velocity. With the last plot, shown in Figure 9(e), the cycle is concluded and the flow field is characterized by the same system of waves as in Figure 9(a).

The analysis of Figure 9 provides some hints on the time history presented in Figures 5 and 6. It can be noted that no shock wave of strong intensity reaches the probe abscissa ($x = 0.508$ m) and this explains the absence of a steep front in the signal. Moreover, the RF has been assumed to be distributed in a quite large region whose position is fixed in time while in the real case, the flame is a thin region moving in the flow field. Again it must be considered that at present the simulation is trying to rebuild the multidimensional numerical solution rather than the experiment. In fact, the experimental data show a steeper front even at $x = 0.508$ m axial position. Although the comparison with experimental data will be the subject of a future step of the study, it can be emphasized here that the existence of steeper fronts within the post, justified in the present study by the occurrence of strong shock waves, has been also found experimentally.[9]

5. Sensitivity analysis to RF parameters

A sensitivity analysis is carried out for both pressure and velocity time-lag RF main parameters in order to understand the effect of each one on the solution and to investigate the model robustness.

5.1. Pressure time-lag RF

Before discussing the results of parametric analysis some clarifications have to be made about the evaluation of mean pressure appearing in equation (9), which expresses the unsteady heat release rate due to coupling between acoustics and combustion as a function of pressure oscillations at the sampling location x_p, corresponding to the back step. In order to identify the fluctuating part of the signal, mean pressure needs to be evaluated. The first approximation consists in considering the mean pressure at limit cycle coincident to the steady-state pressure. This simplification does not hold in the present test case since in nonlinear regime it is not possible to apply the superimposition of effects and mean pressure can change because of fluctuations and eventually lead to an additional heat release content in time, rather than to a term controlled by pressure variation in time. For this reason a mean pressure value changing at runtime is computed suitably filtering the pressure signal. In particular, pressure signal at the back step has been Fourier transformed, setting to zero the coefficients associated to high frequencies. Inverse Fourier transform is then applied and mean pressure is recovered as the low frequency contribution, to be subtracted to the original signal. To select the low-pass filtering frequency different values have been considered. Results are shown in Figure 10. The analysis suggests 510 Hz as the optimum upper limit. In fact suppressing frequencies up to 210 Hz, spurious, nonphysical oscillations are introduced in the signal and their magnitude reduces as the upper limit is increased. If the filter cuts frequency up to 920 Hz, pressure oscillation amplitude is dramatically reduced, indicating that a significant part of the signal has been canceled and not considered as a contribution to the coupling with heat release rate.

The parametric analysis on α_p has considered values from 1960 m/s (the value of Table 3) up to the value that can be handled successfully by the solver that is 3185 m/s. In fact, for the purpose of robustness

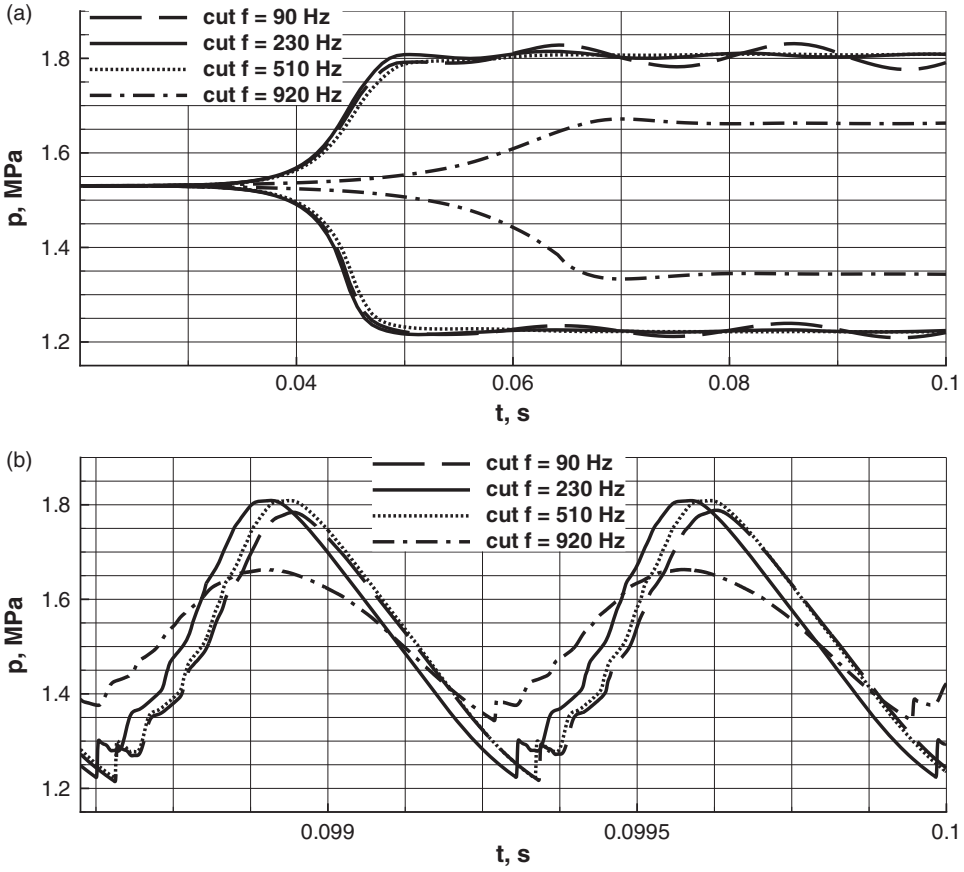

Figure 10. Pressure time-lag response function. Simulations carried out with the same response function parameters and different filter bandwidth. (a) Parametric study on the filter bandwidth. Limit cycle envelopes and (b) zoom on limit cycle.

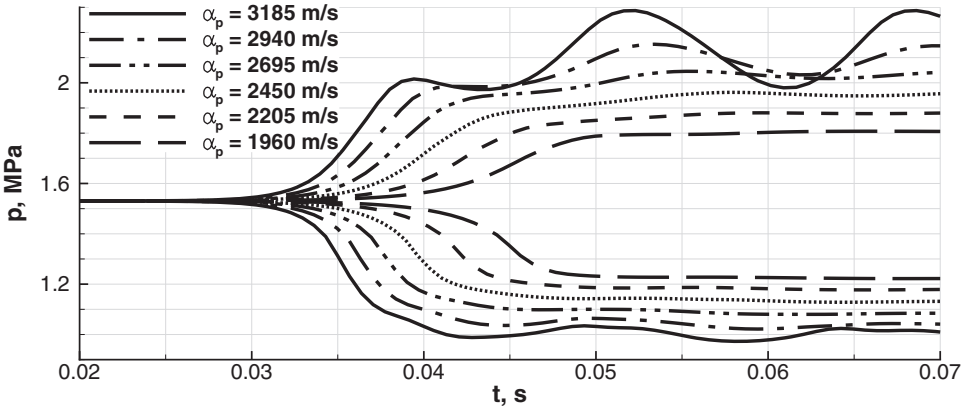

Figure 11. Pressure time-lag response function. Parametric analysis on α_p. Limit cycle envelopes.

investigation, growing values of α could be capable of posing numerical issues. Results are shown in Figure 11 where the role of α_p is quite evident. The parameter affects both amplitude of limit cycle and growth rate. Moreover, increasing α_p it is possible to observe overshoots in the limit cycle envelope.

For $\alpha_p > 3185$ m/s the solver is not able to converge to a physical solution since velocity becomes negative at the left boundary, where a mass flow rate boundary condition is imposed. In experiments, if pressure oscillation amplitude exceeds a certain limit, it is not possible to assume that injection of propellants is occurring

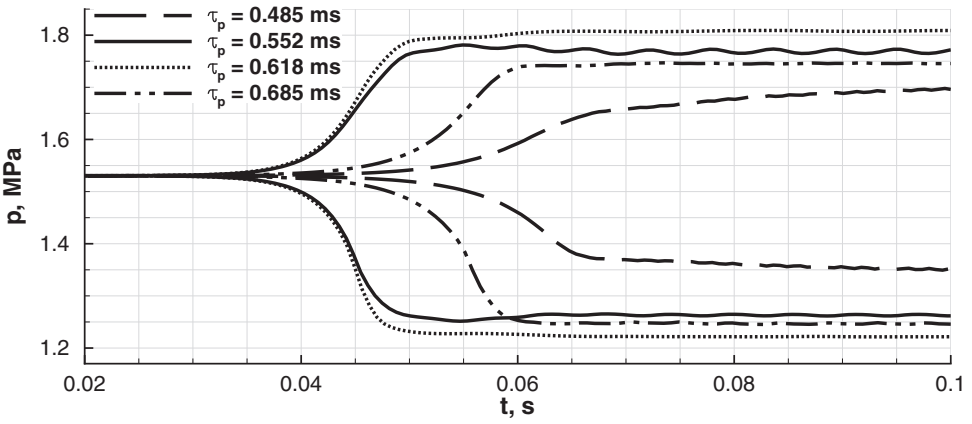

Figure 12. Pressure time-lag response function. Parametric analysis on τ_p. Limit cycle envelopes of the unstable test cases.

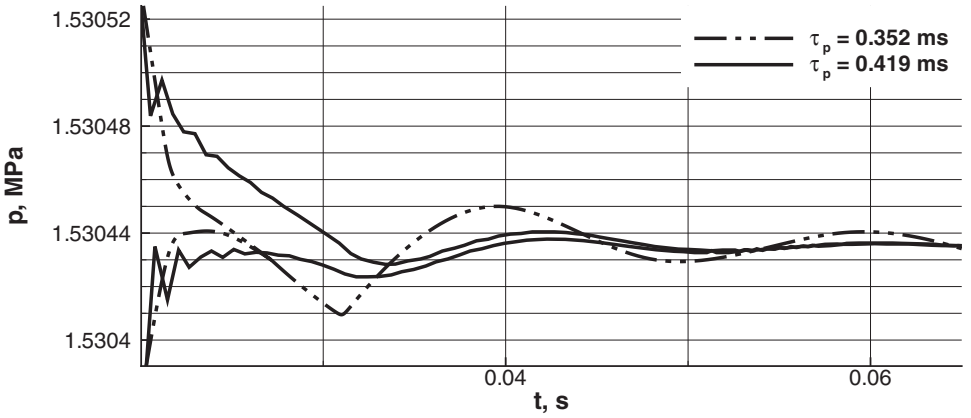

Figure 13. Pressure time-lag response function. Parametric analysis on τ_p. Limit cycle envelopes of the stable test cases.

in choked conditions. For this reason, fixing the mass flow rate in such conditions would be in contrast with the physical phenomenon. Considering that the achievable amplitude is quite beyond the value observed in experimental conditions (see Sardeshmukh et al.[27]), it is possible to conclude that the achievable range is totally acceptable.

The results of the parametric analysis on τ_p are reported in Figures 12 and 13 (see Frezzotti et al.[25,26]). Also the parameter τ_p has an effect on oscillation amplitude but the magnitude of such effect is quite lower than that observed changing α_p. Moreover, some damped cases can be observed. The low frequency oscillations in the decay phase are most likely due to filtering process.

5.2. Velocity time-lag RF

The main difference between velocity and pressure time-lag RFs is that for the former it is possible to assume steady-state velocity as mean value at limit cycle, without filtering the signal to estimate $\bar{u}(x_u)$. The possibility to adopt this simplifying hypothesis is a consequence of the fact that the mean value of velocity does not change significantly, even in nonlinear regime, as shown in Figure 14. The parametric analysis on α_u and τ_u leads to the results shown in Figures 15 to 17.

As observed for the pressure time-lag RF, both parameters are able to modify the amplitude of limit cycle but the magnitude of this effect is much higher in the case of α_u. Moreover, if α_u is increased, growth rates increase too and overshoots are observed. The peak-to-peak distance appears to remain symmetric while this is not the case for τ_u values corresponding to unstable cases. Instability is observed for $0.339\,\text{ms} < \tau_u < 0.605\,\text{ms}$ while for $\tau < 0.399\,\text{ms}$ or $\tau > 0.605\,\text{ms}$, the initial disturbance is damped, yielding to stable behavior. Oscillations appear to decrease in amplitude following an exponential curve, according to linear theory. This observation confirms that low frequency oscillations observed in Figure 13 are due to the filter.

For velocity time-lag response, effects produced by Gaussian standard deviation (σ_u) variations have been

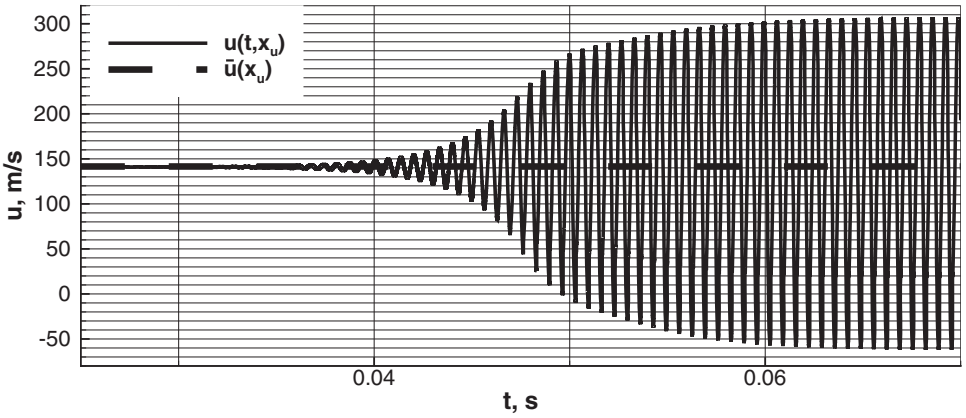

Figure 14. Velocity at the sampling location x_u. Comparison with the time averaged value $\bar{u}(x_u)$

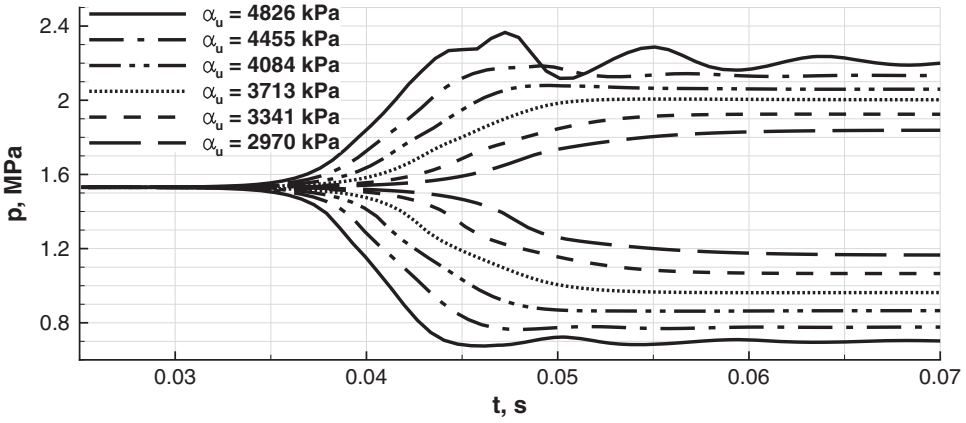

Figure 15. Velocity time-lag response function. Parametric analysis on α_u. Limit cycle envelopes.

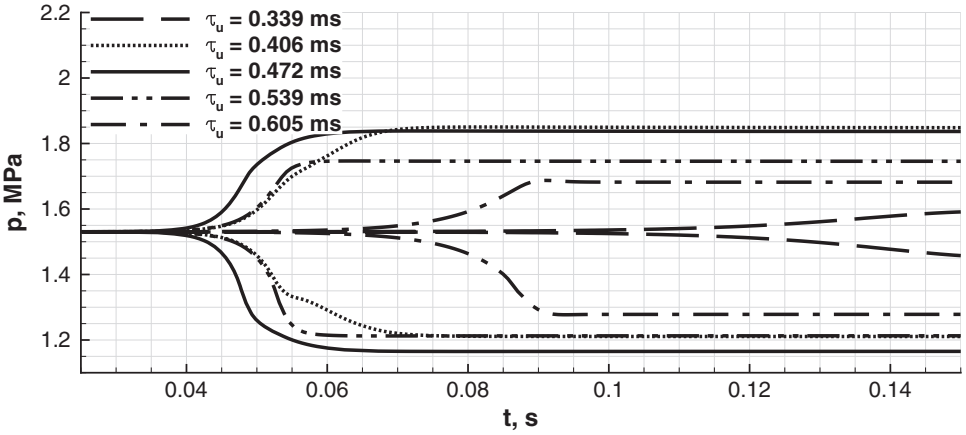

Figure 16. Velocity time-lag response function. Parametric analysis on τ_u. Limit cycle envelopes of the unstable test cases.

investigated. In varying σ_u the integral value of the shape function is kept constant. Nevertheless, as shown in Figure 18, as the Gaussian becomes narrower, the amplitude of limit cycle grows. This behavior can be explained considering that a higher value of σ_u corresponds to a more distributed heat release and, consequently, to a lower peak value. Moreover, the Gaussian mean value μ is quite close to pressure antinode for the

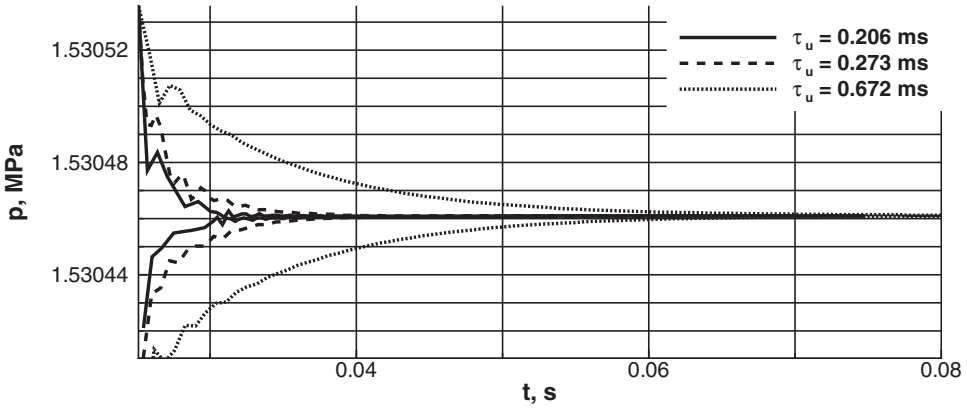

Figure 17. Velocity time-lag response function. Parametric analysis on τ_u. Limit cycle envelopes of the stable test cases.

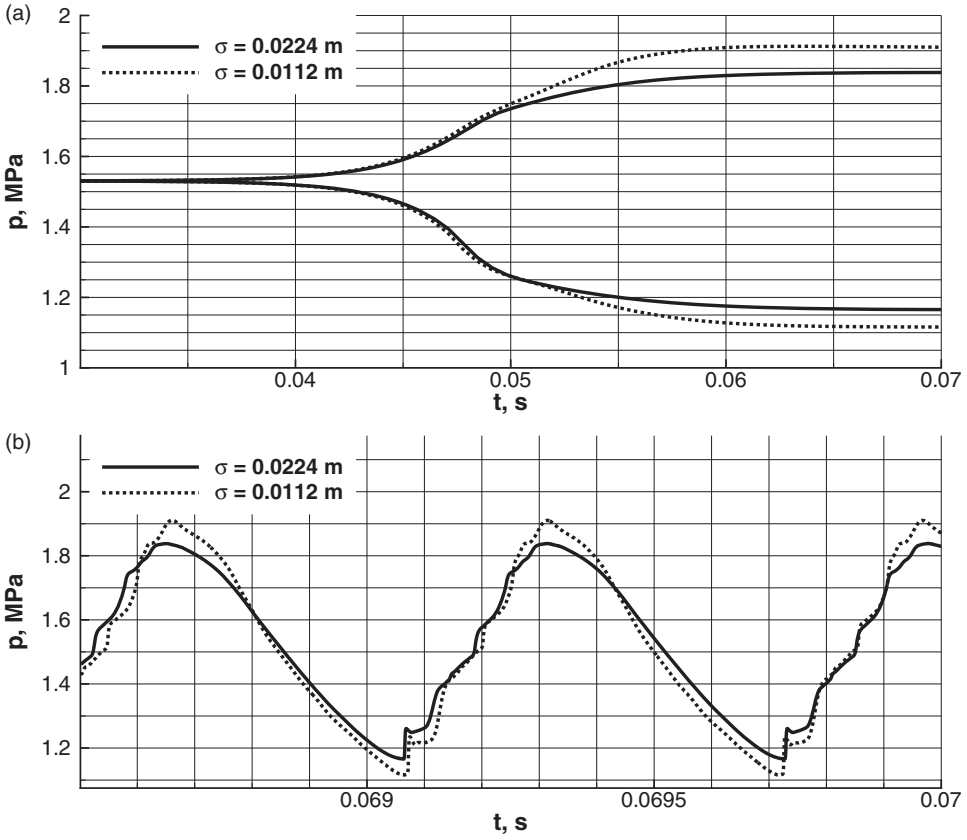

Figure 18. Velocity time-lag response function. Parametric analysis on σ. (a) Limit cycle envelope and (b) enlargement on pressure signals.

first longitudinal frequency and the σ_u value is able to affect the space tuning between pressure and heat release. Figure 18 shows that if the standard deviation is reduced to 50%, the amplitude of limit cycle is about 0.1 MPa higher. This observation leads to the conclusion that a reasonable approximation of σ_u is sufficient to obtain a good estimation of the limit cycle, since the sensitivity of the system with respect to σ_u is quite low.

6. Conclusions

In the present work several numerical issues related to simulations of combustion instability by quasi-1D modeling have been identified and discussed. First of all, ST and MOT models have been compared in terms of capability of representing multispecies problems. Although relevant differences can be observed in the

solution of a contact discontinuity problem for multi-species, comparison between MOT and ST for the CVRC test case yields similar results. The main reason is the similarity in thermodynamical properties of the considered species. This confirms the validity of MOT model as a general approach that could improve results in a case where a different propellant combination may lead to a higher difference in the thermodynamic properties of oxidizer and combustion products, as shown for the case of contact discontinuity, for oxygen and hydrogen.

Pressure and velocity time-lag RFs have been considered. The main difference between the two is the necessity for the former of estimating the mean pressure through a filtering process based on Fourier transform that may alter the features of nonlinear pressure signal, especially before the onset of periodic limit cycle. In this sense, velocity time-lag formulation has to be preferred in this particular application. It is noteworthy that pressure sampling position, x_p, differently from x_u, is in the region where source terms and heat release RF are not null. Given this consideration, the variation of average pressure might be due to the chosen sampling location.

The sensitivity to the main parameters characterizing the RF has been studied, as that of the intensity index and time lag. Both intensity index and time-lag parameters are able to modify the amplitude of limit cycle. Damped conditions can be reproduced for specific ranges of time lag. The range of variation of the parameters allowed by the solver is adequate to implement RFs estimated from high fidelity simulations and to reach amplitudes of limit cycle comparable with experiments. Finally, sensitivity to the selected value of the standard deviation of the Gaussian shape function has been analyzed. The analysis has shown how a narrower distribution allows for higher amplitude of limit cycle, since the spatial tuning between pressure and heat release rate is increased.

Declaration of Conflicting Interests

The author(s) declared no potential conflicts of interest with respect to the research, authorship, and/or publication of this article.

Funding

The author(s) received no financial support for the research, authorship, and/or publication of this article.

References

1. Oefelein JC and Yang V. Comprehensive review of liquid-propellant combustion instabilities in F-1 engines. *J Propul Power* 1993; 9(5): 657–677.
2. Yu YC, Koeglmeier SM, Sisco JC, et al. Combustion instability of gaseous fuels in a continuously variable resonance chamber (CVRC). In: *Forty-fourth AIAA/ASME/SAE/ASEE joint propulsion conference and exhibit*, Hartford, CT, 21–23 July 2008, pp.1–12. Reston, VA, USA: American Institute of Aeronautics and Astronautics.
3. Sisco JC, Portillo JE, Yu YC, et al. Non-linear characteristic of longitudinal instabilities in a model rocket combustor. In: *Forty-third AIAA/ASME/SAE/ASEE joint propulsion conference and exhibit,* Cincinnati, OH, USA, 8–11 July 2007, pp.1–16. Reston, VA, USA: American Institute of Aeronautics and Astronautics.
4. Durox D, Schuller T, Noray N, et al. Experimental analysis of nonlinear flame transfer functions for different flame geometries. *Proc Combus Inst* 2009; 32: 1391–1398.
5. Wierman M, Feldman T and Anderson W. Development of combustion response function in a subscale high pressure longitudinal combustor. In: *Forty-ninth AIAA/ASME/SAE/ASEE joint propulsion conference*, San Jose, CA, USA, 14–17 July 2013, pp 1–14. Reston, VA, USA: American Institute of Aeronautics and Astronautics.
6. Smith R, Ellis M, Xia G, et al. Computational investigation of acoustics and instabilities in a longitudinal-mode rocket combustor. *AIAA J* 2008; 46: 2659–2673.
7. Yu YC, O'Hara L, Sisco JC, et al. Experimental Study of High-Frequency Combustion Instability in a Continuously Variable Resonance Combustor (CVRC). In: *Forty-seventh AIAA aerospace sciences meeting including the new horizons forum and aerospace expositions*, Orlando, FL, USA, 5–8 January 2009, pp.1–12. Reston, VA, USA: American Institute of Aeronautics and Astronautics.
8. Garby R, Selle L and Poinsot T. Analysis of the impact of heat losses on an unstable model rocket-engine combustor using large eddy simulation. In: *Forty-eighth AIAA/ASME/SAE/ASEE joint propulsion conference and exhibit*, Atlanta, GA, USA, 30 July–1 August 2012, pp.1–5. Reston, VA, USA: American Institute of Aeronautics and Astronautics.
9. Yu YC, Sisco JC, Rosen S, et al. Spontaneous longitudinal combustion instability in a continuously-variable resonance combustor. *J Propul Power* 2012; 28: 876–887.
10. Harvazinski ME, Huang C, Sankaran V, et al. Combustion instability mechanisms in a pressure-coupled gas-gas coaxial rocket injector. In: *Forty-ninth AIAA/ASME/SAE/ASEE joint propulsion conference*, San Jose, CA, USA, 14–17 July 2013, pp.1–21. Reston, VA, USA: American Institute of Aeronautics and Astronautics.
11. Harvazinski ME. *Modeling of self-excited combustion instabilities using a combination of two- and three-dimensional simulations*. PhD Thesis, Purdue University, Purdue e-Pubs, West Lafayette, IN, USA, 2012, http://search.proquest.com/docview/1238240720.
12. Garby R. *Simulations of flame stabilization and stability in high-pressure propulsion systems*. PhD Thesis, Universit de Toulouse, Institut National Polytechnique de Toulouse, Toulouse, France, 2013, http://ethesis.inp-toulouse.fr/archive/00002392/01/garby.pdf.

13. McBride BJ and Gordon S. *Computer program for calculation of complex chemical equilibrium compositions and applications*. NASA Reference Publication 1311, 1994.
14. Law CK. *Combustion physics*. New York, USA: Cambridge University Press, 2006.
15. Crocco L and Cheng SI. *Theory of combustion instability in liquid propellant rocket motors*. AGARD Monograph No. 8, Published for and on behalf of the Advisory group for aeronautical research and development north Atlantic treaty organization by Butterworths Scientific Publication. Belfast, Northern Ireland: The University Press, 1956.
16. Chong LTW, Kaess R, Komarek T, et al. Identification of flame transfer function from LES of turbulent reacting flows. In: Wagner S, et al. (eds) *High performance computing in science and engineering* Garching/Munich, 2010, pp.255–266. Germany: Springer-Verlag Berlin.
17. Chong LTW, Komarek T, Kaess R, et al. Identification of flame transfer function from LES of a premixed swirl burner. In: *ASME turbo expo 2010: power for land, sea and air*, Glasgow, UK, 14–18 June 2010, pp.1–13. ASME.
18. Krediet HJ, Beck CH, Krebs W, et al. Identification of the flame describing function of a premixed swirl flame from LES. *Combus Sci Technol* 2012; 184: 888–900.
19. Abgrall R. How to prevent pressure oscillations in multicomponent flow calculations: a quasi conservative approach. *J Comput Phys* 1996; 125: 150–160.
20. Sassu D. *Modelli termodinamici discreti per sistemi iperbolici miscele di gas ideali*. Master Thesis, Sapienza, University of Rome, Biblioteca di Ingegneria Meccanica e Aerospaziale, Facoltà di ingegneria, Università La Sapienza, Roma, 2012.
21. Gottlieb JJ and Groth CPT. Assessment of Riemann solvers for unsteady one-dimensional inviscid flows of perfect gases. *J Comput Phys* 1988; 78: 437–458.
22. Toro EF. *Riemann solvers and numerical methods for fluid dynamics*. Germany: Springer-Verlang Berlin, 2009.
23. Selle L, Blouquin R, Thron M, et al. Prediction and analysis of combustion instabilities in a model rocket engine. *J Propul Power* 2014; 30: 978–990.
24. Roache PJ. Verication of codes and calculations. *AIAA J* 1998; 36: 696–702.
25. Frezzotti ML, Nasuti F, Huang C, et al. Response function modeling in the study of longitudinal combustion instability by a Quasi-1D eulerian solver. In: *Fifty-first AIAA/ASME/SAE/ASEE joint propulsion conference*, Orlando, FL, USA, 27–29 July 2015, pp.1–13. Reston, VA, USA: American Institute of Aeronautics and Astrnautics.
26. Frezzotti ML, Nasuti F, Huang C, et al. Determination of heat release response function from 2D hybrid RANS-LES data for the CVRC combustor. In: *Fifty-first AIAA/ASME/SAE/ASEE joint propulsion conference*, Orlando, FL, USA, 27–29 July 2015, pp.1–13. Reston, VA, USA: American Institute of Aeronautics and Astronautics.
27. Sardeshmukh SV, Anderson WE, Harvazinski ME, et al. Prediction of combustion instability with detailed chemical kinetics. In: *Fifty-third AIAA aerospace science meeting*, Kissimmee, FL, USA, 5–9 January 2015, pp.1–19. Reston, VA, USA: American Institute of Aeronautics and Astronautics.